Acta Crystallographica Section B
Structural Science
ISSN 0108-7681

Theoretical determination of the structures of $CaSiO_3$ perovskites

Razvan Caracas*‡ and Renata M. Wentzcovitch§

University of Minnesota, Department of Chemical Engineering and Material Science, 421 Washington Avenue, Minneapolis, MN 55455, USA

‡ Present address: Geophysical Laboratory, Carnegie Institution of Washington, 5251 Broad Branch Road N.W., Washington, DC 20015, USA.
§ Present address: Bayerisches Geoinstitut, University of Bayreuth, Universitaetstrasse 30, D-95447 Bayreuth, Germany.

Correspondence e-mail: r.caracas@gl.ciw.edu

Received 31 August 2006
Accepted 4 September 2006

Density functional theory is used to determine the possible crystal structure of the $CaSiO_3$ perovskites and their evolution under pressure. The ideal cubic perovskite is considered as a starting point for studying several possible lower-symmetry distorted structures. The theoretical lattice parameters and the atomic coordinates for all the structures are determined, and the results are discussed with respect to experimental data.

1. Introduction

$CaSiO_3$ is the third most important component of the Earth's lower mantle, where, according to the current geophysical models, it can account for as much as 7% in volume (Ringwood, 1975; O'Neill & Jeanloz, 1990; Ita & Stixrude, 1992). Above 10 GPa and 1100 K, $CaSiO_3$ has the ideal cubic perovskite structure (Gasparik *et al.*, 1994; Swamy & Dubrovinsky, 1997; Shim *et al.*, 2000) with $Pm\bar{3}m$ symmetry.

This phase is unquenchable, and at ambient conditions of temperature and pressure it becomes amorphous (*e.g.* Liu & Ringwood, 1975; Wang & Weidner, 1994). According to different experimental studies (Shim *et al.*, 2002) and theoretical calculations (Stixrude *et al.*, 1996; Chizmeshya *et al.*, 1996; Akber-Knutson *et al.*, 2002; Magyari-Köpe *et al.*, 2002; Jung & Oganov, 2005), at low temperature, $CaSiO_3$ has a distorted-perovskite structure, several tetragonal and orthorhombic candidates being proposed. However, no structural refinement of these possible modifications has been performed to date, and there are still controversies related to the symmetry of these phases.

In our previous paper (Caracas *et al.*, 2005), we reported on the implications of $CaSiO_3$ in modeling the Earth's lower mantle, while in the present study we present a detailed analysis of the crystallochemistry of $CaSiO_3$ perovskites. We start our analysis with the investigation of the phonon band dispersions in the cubic phase at different pressures. We find that the cubic structure exhibits unstable phonon modes at the zone boundary, appearing between the high-symmetry points R {1/2, 1/2, 1/2} and M {1/2, 1/2, 0}. The instability of the cubic phase increases with pressure, the frequency of the unstable phonon at R decreasing from $150i$ cm^{-1} at -5 GPa to $221i$ cm^{-1} at 164 GPa. The frequency of the LO (longitudinal optic) unstable phonon at M slightly increases from $109i$ cm^{-1} at -5 GPa to $99i$ cm^{-1} at 164 GPa. These unstable modes are characterized by rotations of octahedra in columns parallel to the Cartesian axes. The unstable mode at M corresponds to in-phase rotations, where all the octahedra in one column rotate in the same direction, while the unstable mode at R corresponds to out-of-phase rotations, where each octahedron rotates contrary to all its neighbors. According to Glazer's (1972, 1975) notation, the first type of rotation, in-phase, is

Table 1
Derivation of the distorted perovskite structures, the corresponding Glazer notation, the number of molecules within the conventional unit cell, Z, the unit-cell relation with respect to the cubic parent one, the grid of special **k**-points and the grid shifts used in our calculations.

Symmetry	Phonons	Rotations	Z	Supercell	**k**-points grid	Grid shifts
$Pm\bar{3}m$	–	$a^0a^0a^0$	1	$1 \times 1 \times 1$	$4 \times 4 \times 4$	0.5 0.5 0.5
$I4/mcm$	R	$a^0a^0c^-$	4	$2^{1/2} \times 2^{1/2} \times 2$	$2 \times 2 \times 2$	0.5 0.0 0.5 0.0 0.5 0.5
$Imma$	R,R	$a^0b^-b^-$	4	$2^{1/2} \times 2^{1/2} \times 2$	$2 \times 2 \times 2$	0.5 0.0 0.5 0.0 0.5 0.5
$P4/mbm$	M	$a^0a^0c^+$	2	$2^{1/2} \times 2^{1/2} \times 2$	$2 \times 2 \times 4$	0.5 0.0 0.5 0.0 0.5 0.5
$I4/mmm$	M,M	$a^0b^+b^+$	8	$2 \times 2 \times 2$	$2 \times 2 \times 2$	0.5 0.5 0.5
$Im\bar{3}$	M,M,M	$a^+a^+a^+$	8	$2 \times 2 \times 2$	$2 \times 2 \times 2$	0.5 0.5 0.5
$P42nmc$	M,M,R	$a^+a^+c^-$	8	$2 \times 2 \times 2$	$2 \times 2 \times 2$	0.5 0.5 0.5
$Pnma$	R,R,M	$a^-a^-c^+$	4	$2^{1/2} \times 2^{1/2} \times 2$	$2 \times 2 \times 2$	0.5 0.5 0.0

Table 2
Special atomic positions in $CaSiO_3$ perovskites.

Symmetry	Space group	Ca	Si	O
$Pm\bar{3}m$	221	1(*b*) (0.5 0.5 0.5)	1(*a*) (0 0 0)	3(*d*) (0.5 0 0)
$I4/mcm$	140	4(*b*) (0 0.5 0.25)	4(*c*) (0 0 0)	4(*a*) (0 0 0.25) 8(*h*) (*x x*+0.5 0.0)
$Imma$	74	4(*e*) (0 0.25 *z*)	4(*a*) (0 0 0)	8(*g*) (0.25 *y* 0.25) 4(*e*) (0 0.25 *z*)
$P4/mbm$	127	2(*c*) (0 0.5 0.5)	2(*a*) (0 0 0)	2(*b*) (0 0 0.5) 4(*g*) (*x x*+0.5 0)
$I4/mmm$	139	2(*a*) (0 0 0) 2(*b*) (0 0 0.5) 4(*c*) (0 0.5 0)	8(*f*) (0.25 0.25 0.25)	8(*h*) (*x x* 0) 16(*n*) (0 *y z*)
$Im\bar{3}$	204	2(*a*) (0 0 0) 6(*b*) (0 0.5 0.5)	8(*c*) (0.25 0.25 0.25)	24(*g*) (0 *y z*)
$P4_2/nmc$	137	2(*a*) (0.75 0.25 0.75) 2(*b*) (0.75 0.25 0.25) 4(*d*) (0.25 0.25 0.25 + *z*)	8(*e*) (0 0 0)	8(*f*) (*x* −*x* 0.25) 8(*g*) (0.25 *y z*) 8(*g*) (0.75 *y* 0.5+*z*)
$Pnma$	62	4(*c*) (*x* 0.25 *z*)	4(*a*) (0 0 0)	8(*d*) (*x y z*) 4(*c*) (*x* 0.25 *z*)

designated by a plus sign, and the second, out-of-phase, by a minus sign. Consequently, the $a^+b^-c^0$ notation represents the superposition of an in-phase rotation around the a axis and an out-of-phase rotation around the b axis, with different amplitudes. There is no rotation around the c axis. This notation corresponds to a structure derived by the simultaneous condensation of one unstable phonon at R and one at M. Glazer (1972, 1975) built all the possible distorted perovskite structures based on such rigid octahedral rotations, obtaining 26 structures by combining up to three out-of-phase and/or in-phase rotations.

Further improvements of Glazer's model were realized by taking into account the group–subgroup relations between the distorted structures (Howard & Stokes, 1998), or by considering only those generated by rotations of the same magnitude around equivalent axes (Darlington, 2002). We base our exploration of the distorted structures of $CaSiO_3$ perovskite on the approach proposed by Darlington (2002). Our analysis is thus limited only to the structures that may result from the condensation of the unstable phonon modes at R and M, the largest distorted cell being a $2 \times 2 \times 2$ supercell ($Z = 8$) of the cubic structure (Table 1). All the theoretical structures listed in Table 1 are energetically competitive and at high pressure slightly lower than the cubic $Pm\bar{3}$ phase. Condensations of unstable phonon modes at points other than M and R are certainly possible at any arbitrary commensurate and/or incommensurate points on the MR line. However, based on our results, we do not expect a major energy lowering due to such condensations.

2. Computational details

All the calculations are based on the local density approximation of the density functional theory (Hohenberg & Kohn, 1964; Kohn & Sham, 1965), as implemented in the *PWSCF* code (Baroni *et al.*, 2001). The *PWSCF* code is based on plane waves and pseudopotentials. Within this approach, the wavefunctions describe only the valence and conduction electrons, while the core electrons are taken into account using pseudopotentials. We use Troullier–Martins pseudopotentials, whose construction details and reference electronic configurations are published elsewhere (Karki & Wentzcovitch, 2003).

We determine the crystal structures using variable-cell-shape molecular dynamics (Wentzcovitch, 1991). This method allows the simultaneous determination of both the unit-cell parameters and the internal degrees of freedom (atomic coordinates) within an *ab initio* approach. A fictitious mass is attributed to the unit cell in order to apply the molecular dynamics technique to both the cell and the atoms. Here these dynamics are used in the damped form to search for the lowest enthalpy configurations. We fully relax the lattice parameters and the atomic positions. The initially chosen space-group symmetries are naturally preserved during the relaxation process leading to the final lattice parameter and Wyckoff coordinates.

We use an 85 Rydberg (1 Rydberg = 13.605 eV) cut-off radius for the plane-wave kinetic energy. The sampling of the parent cubic Brillouin zone (BZ) is achieved by using a primitive $4 \times 4 \times 4$ grid of special **k** points (Monkhorst & Pack, 1976). These parameters ensure an accuracy of the calculations of better than 5 kbar in pressure and of the order of 10 meV per molecule in energy. As we study different structures, all derived from the cubic one, we use in all our calculations BZ sampling schemes that are equivalent to the $4 \times 4 \times 4$ grid of **k** points of the parent cubic structure. The relation between the BZs follows the group–subgroup relation

that exists between the parent cubic and each of these lower-symmetry structures. As they represent superstructures of the cubic lattice, their BZ will be smaller than the parent cubic one. Some of the **k** points from the first cubic BZ will find themselves in the second BZ of the superstructure. Consequently, these points will be folded back to the first BZ of the superstructure. The high symmetry of the starting grid that samples the parent cubic structure and the position of the BZs of the superstructures with respect to the cubic one ensure the superposition of the **k** points during folding, and thus a smaller number of **k** points in the superstructure is needed. The resulting **k**-point grids in the superstructures may be described as several superposed grids, a common technique that allows a maximum sampling of the BZ with a minimum cost (Froyen, 1992). This procedure also guarantees the accuracy and the meaningfulness of the comparison between the different polymorphs, as the reciprocal space is equally well sampled in all the structures. The **k**-point grids used for each structure and their shifts with respect to Γ are given in Table 1, while Fig. 1 presents a simplified model of their reduction.

3. Results and discussion

All the cubic, tetragonal and orthorhombic structures obtained from condensation of the unstable phonon modes in *R* and *M* have energy lower than or comparable to the ideal cubic perovskite phase (at 160 GPa, the energy of the *I*4/*mcm* structure that is the most stable is about 90 meV per molecule below the energy of the cubic structure). These structures are characterized by slight distortions, induced by the almost rigid rotating octahedra. The structural resemblance of these structures with the parent cubic phase, together with inherent kinetic factors, made their experimental identification a difficult task (Shim *et al.*, 2002).

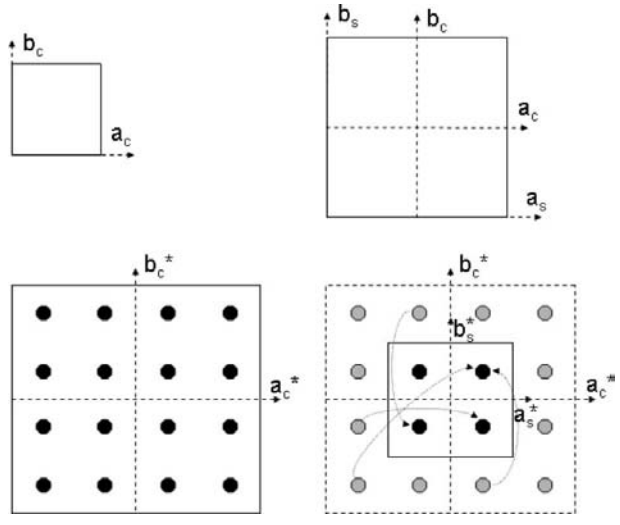

Figure 1
Simple two-dimensional model of the relations between the Brillouin zones of a parent structure and a derived superstructure, and the folding of the **k** points from the second to the first BZ of the superstructure.

Our theoretical results are summarized in Tables 2 and 3. Table 2 lists the Wyckoff positions occupied by Ca, Si and O atoms in each of the analyzed structures, while the evolution with pressure of the internal degrees of freedom (positions not fixed by symmetry) and of the lattice parameters is given in Table 3. As an example, the crystal structures of the lowest-energy polymorphs, *I*4/*mcm*, $P4_2/nmc$ and *Pnma*, are presented in Fig. 2.

The experimental measurements (Shim *et al.*, 2002) show lattice distortions corresponding to tetragonal structures associated with *c*/*a* ratios slightly smaller than 1.0. According to our theoretical results, all tetragonal structures, except *I*4/*mmm*, have *c*/*a* ratios slightly larger than 1.0. The origin of

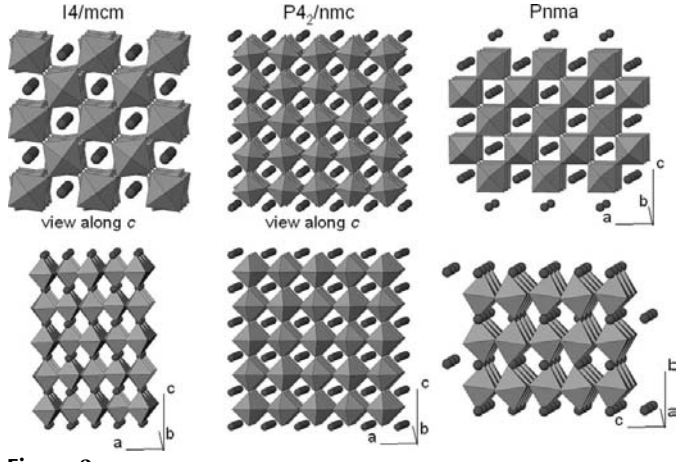

Figure 2
Crystal structure of the lowest-energy distorted modifications of $CaSiO_3$. The structures in the top row are viewed along the *b* axis, with *a* horizontal, and those in the lower row along the *a* axis, with *c* horizontal. From left to right, the structures of the *I*4/*mcm*, $P4_2/nmc$ and *Pnma* phases are shown.

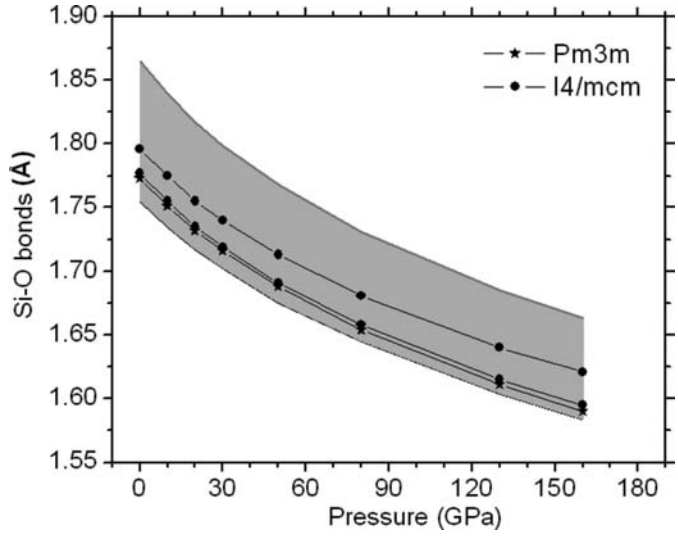

Figure 3
Range of Si—O bond lengths in the cubic, tetragonal and orthorhombic modifications of $CaSiO_3$. The bonds in the cubic $Pm\bar{3}m$ and tetragonal *I*4/*mcm* phases are plotted for comparison.

Table 3
Lattice parameters (in Å) and the general atomic coordinates for the analyzed $CaSiO_3$ perovskites, as determined at different pressures.

P (GPa)	0	10	20	30	50	80	130	160
Pm$\bar{3}$*m*								
a	3.5460	3.5019	3.4648	3.4314	3.3755	3.3082	3.2221	3.1804
I4/*mcm*								
a	4.9812	4.9183	4.8597	4.8160	4.7348	4.6368	4.5111	4.4509
c	7.1820	7.0987	7.0191	6.9611	6.8527	6.7240	6.5607	6.4837
O *x*	0.2164	0.2159	0.2154	0.2149	0.2138	0.2124	0.2102	0.2090
Imma								
a	5.0116	4.9479	4.8945	4.8485	4.7645	4.6671	4.5413	4.4801
b	7.0641	6.9739	6.8988	6.8355	6.7163	6.5802	6.4038	6.3185
c	5.0361	4.9763	4.9243	4.8815	4.8021	4.7112	4.5964	4.5398
Ca *z*	0.0020	0.0017	0.0014	0.0013	0.0010	0.0007	0.0004	0.0002
O1 *y*	0.0228	0.0226	0.0225	0.0225	0.0226	0.0230	0.0238	0.0241
O2 *z*	0.0439	0.0436	0.0435	0.0436	0.0440	0.0447	0.0464	0.0471
*P*4/*mbm*								
a	4.8931	4.8349	4.7846	4.7402	4.6640	4.5717	4.4530	4.3954
c	3.7294	3.6773	3.6348	3.5972	3.5353	3.4620	3.3705	3.3267
O *x*	0.2072	0.2065	0.2059	0.2053	0.2043	0.2030	0.2013	0.2005
*I*4/*mmm*								
a	7.1052	7.0194	6.9057	6.8714	6.7602	6.6205	6.4454	6.3581
c	7.0684	6.9830	6.9422	6.8370	6.7264	6.6007	6.4293	6.3422
O1 *x*	0.2338	0.2344	0.2349	0.2353	0.2360	0.2376	0.2385	0.2389
O2 *x*	0.2504	0.2504	0.2504	0.2504	0.2503	0.2503	0.2502	0.2502
O2 *z*	0.2666	0.2659	0.2654	0.2649	0.2642	0.2626	0.2616	0.2612
*Im*3								
a	7.0933	7.0054	6.9301	6.8640	6.7517	6.6158	6.4443	6.3610
O *y*	0.2627	0.2622	0.2618	0.2613	0.2607	0.2599	0.2587	0.2581
O *z*	0.2367	0.2372	0.2377	0.2382	0.2389	0.2398	0.2411	0.2417
$P4_2/nmc$								
a	7.0476	6.9583	6.8868	6.8139	6.6990	6.5601	6.3818	6.2954
c	7.1764	7.0913	7.0241	6.9557	6.8483	6.7203	6.5590	6.4815
Ca2 *z*	0.2509	0.2510	0.2509	0.2510	0.2509	0.2508	0.2510	0.2501
O1 *x*	0.0014	0.0015	0.0014	0.0016	0.0013	0.0012	0.0015	0.0001
O2 *y*	0.0326	0.0326	0.0326	0.0325	0.0326	0.0325	0.0325	0.0329
O2 *z*	0.0013	0.0014	0.0013	0.0015	0.0012	0.0011	0.0014	0.0001
O3 *y*	0.0326	0.0325	0.0325	0.0325	0.0326	0.0325	0.0325	0.0329
O3 *z*	0.0014	0.0015	0.0014	0.0016	0.0013	0.0012	0.0015	0.0001
Pnma								
a	5.0083	4.9471	4.8934	4.8457	4.7650	4.6670	4.5414	4.4804
b	7.0858	6.9864	6.9049	6.8379	6.7193	6.5803	6.4044	6.3191
c	5.0243	4.9703	4.9214	4.8765	4.8020	4.7112	4.5954	4.5397
Ca *x*	0.5106	0.5072	0.5050	0.5048	0.5025	0.5012	0.5006	0.5004
Ca *z*	0.0022	0.0018	0.0015	0.0013	0.0011	0.0007	0.0004	0.0002
O1 *x*	0.2656	0.2610	0.2580	0.2578	0.2541	0.2519	0.2510	0.2507
O1 *y*	0.0214	0.0219	0.0221	0.0222	0.0225	0.0229	0.0236	0.0241
O1 *z*	0.2344	0.2390	0.2420	0.2423	0.2459	0.2481	0.2490	0.2493
O2 *x*	0.9983	0.9990	0.9994	0.9996	−0.0001	0.0000	0.0001	0.0001
O2 *z*	0.9584	0.9574	0.9570	0.9569	0.9562	0.9553	0.9539	0.9530

the discrepancy could be due to 0 K calculations, as at finite *T* the structure might be partially disordered.

The Si—O bond lengths lie in the range 1.75–1.87 Å at 0 GPa and 1.58–1.67 Å at 160 GPa, as shown in Fig. 3. Both maximum and minimum bonds are recorded in *P*4/*mbm*. Fig. 3 also plots the position of the bonds in *Pm*$\bar{3}$*m* and *I*4/*mcm* with respect to the whole range of computed Si—O lengths. It is interesting to note that even if the tetragonal *I*4/*mcm* modification has a density larger than the cubic *Pm*$\bar{3}$*m*, the Si—O bonds in the former structure are longer than those in the latter. Thus, the higher compaction of the tetragonal phase is realized through octahedral rotations. The difference in bond lengths that reflects an octahedral deformation is about 0.02 Å in *I*4/*mcm*.

Table 4
The positions of the most intense powder diffraction peaks as simulated based on the theoretical structures at 50 GPa.

The experimental values are interpolated from the spectra published by Shim *et al.* (2002). The peak indexation corresponds to *Pm*$\bar{3}$*m*. The 2θ peak position is given in degrees.

Symmetry	110	111	200	210	211
Experimental	17.3	22.3	24.5		30.2
	17.4		24.6		30.3
Pm$\bar{3}$*m*	17.1	21.0	24.3		29.8
*I*4/*mcm*	17.0	20.2	23.9	27.3	29.6
	17.2	21.0	24.5	27.4	30.0
Imma	17.0	20.0	24.2	26.3	29.7
	17.1	20.9	24.4	26.5	29.9
		21.0			30.0
*P*4/*mbm*	16.9	19.6	23.2		29.2
	17.5	21.0	24.6		30.2
					30.5
*I*4/*mmm*	17.1	19.1	22.7	27.1	28.5
	17.1	21.0	24.4	27.2	29.6
			25.7		31.0
*Im*3	17.1	21.0	24.3	27.2	29.8
$P4_2/nmc$	17.0	19.2	23.9	26.9	29.6
	17.2	21.0	24.5	27.3	30.0
Pnma	17.0	20.0	23.2	26.3	29.7
	17.1	20.9	24.4	26.5	29.7
					29.9

The evolution with pressure of the Si—O—Si angles in the distorted structures is shown in Fig. 4. All the angles lie above

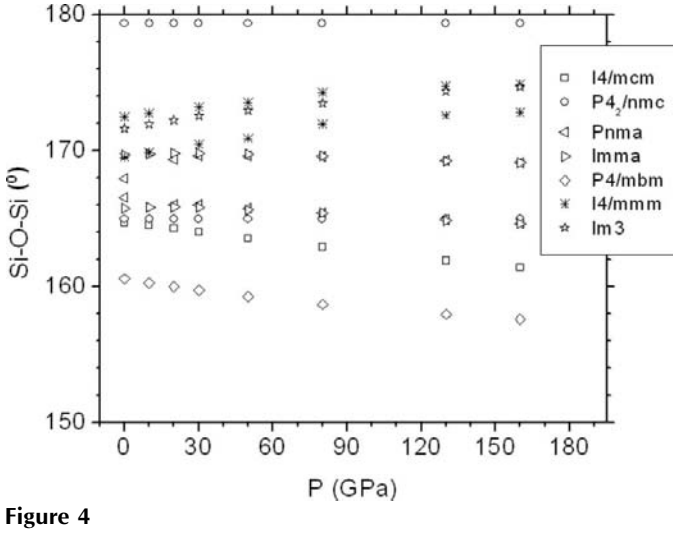

Figure 4
Pressure evolution of the Si—O—Si interatomic angles.

155°, with the relatively weak pressure dependence. The smallest Si—O—Si angles are obtained in *P*4/*mbm* and *I*4/*mcm*, both with a decreasing trend under pressure. The Si—O—Si angles are directly related to the octahedral rotations induced by the phonon instabilities only for pure in-phase and pure out-of-phase rotations in the *P*4/*mbm* and *I*4/*mcm* structures, respectively. In the other cases, the coupling between the unstable phonon modes as well as the lattice deformations allow us only to estimate the octahedral rotations to less than 8°.

Based on the theoretically determined crystal structures we may simulate the powder diffraction pattern and compare it with the experimental data. The experimental powder diffraction pattern (Shim *et al.*, 2002) recorded at 45.8 GPa shows weak splittings of the 110, 200 and 211 cubic peaks occurring around 2θ = 17.4, 24.6 and 30.3°, respectively. Fig. 5 shows the simulated powder diffraction patterns for 2θ ranging between 15 and 32.5° at 50 GPa for all the studied structures, while Table 4 details the positions of the most intense peaks. The *I*4/*mmm* structure shows the most complex diffraction pattern, while the cubic *Im*3 phase, because of the symmetry, does not show any splitting. The *P*4/*mbm* tetragonal phase exhibits a large splitting of the cubic 200 peak. In the orthorhombic phases, *Pnma* and *Imma*, the peak splittings are small and they contribute mainly to the peak broadening. The other tetragonal phases, *I*4/*mcm*, *P*4/*mbm* and $P4_2/nmc$, exhibit large splittings.

In general, with respect to the experimental pattern we observe various differences in the splitting magnitude and the peak intensity for all the theoretical structures. These discrepancies are associated with theoretical distortions from the ideal cubic symmetry that are larger than the experimental ones, owing to the neglect of the thermal effects in our calculations and the presence of dynamical or static disorder exhibited by the SiO_6 octahedra in the real structure of $CaSiO_3$. However, the theoretical structures we report in this study can be used as starting points in the structural refinements of the $CaSiO_3$ perovskite structure. The detailed theoretical analysis of the different possible space groups and of the distortions associated with these represent an important input for experimentalists attempting to solve the structures of $CaSiO_3$ perovskites at high pressures and temperatures from diffraction data.

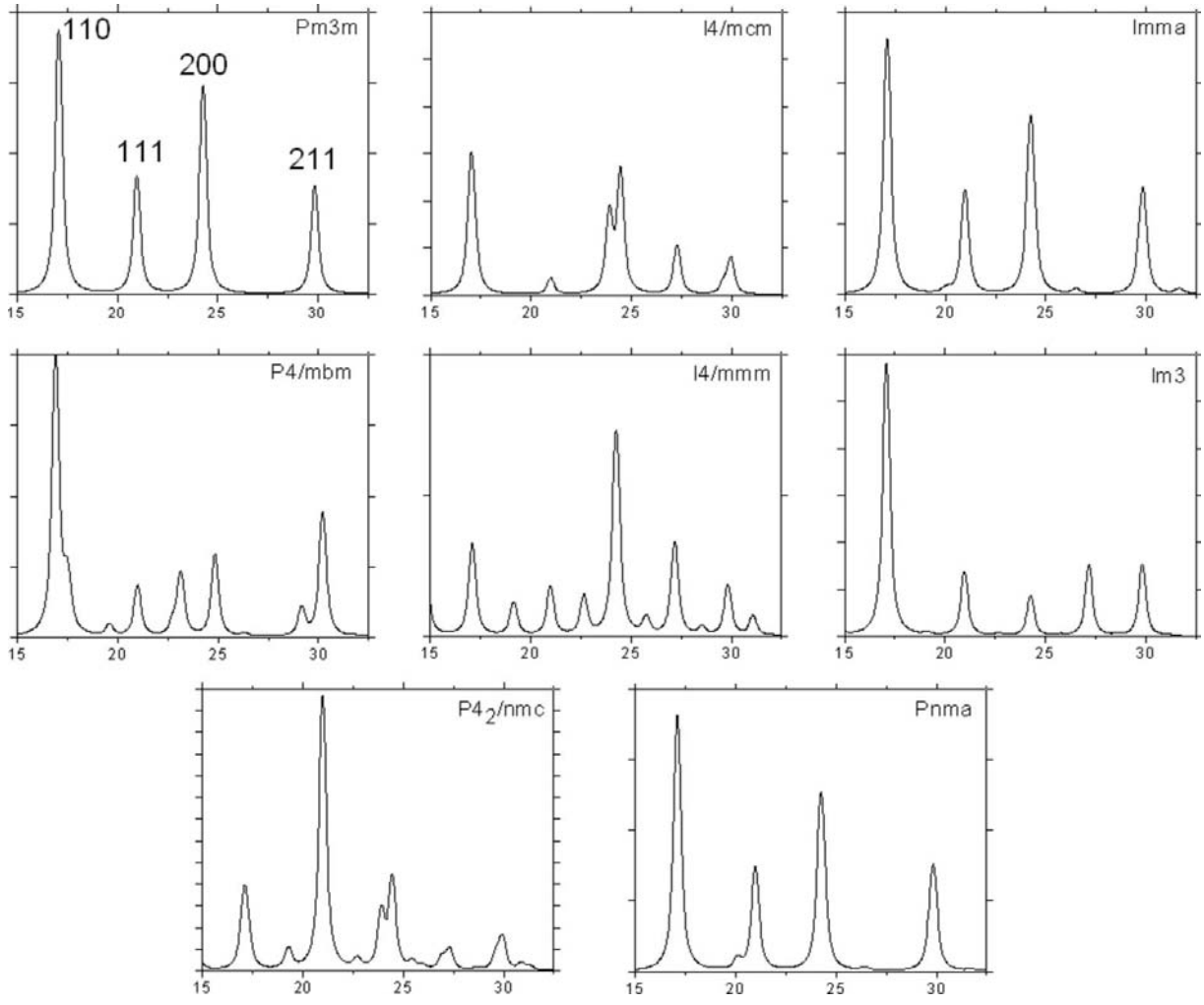

Figure 5
Theoretical powder diffraction patterns for different polymorphs of the $CaSiO_3$ perovskite.

Calculations were performed using the *PWSCF* package, http://www.pwscf.org, which is now part of the *Quantum-ESPRESSO* package (opEn-Source Package for Research in Electronic Structure, Simulation, and Optimization; http://www.quantumespresso.org). This is an initiative of the DEMOCRITOS National Simulation Centre (http://www.democritos.it) for the development of open-source scientific software. This research was supported by the NSF grants EAR-0135533 and EAR-0230319, and the Minnesota Supercomputing Institute. We thank B. B. Karki for the pseudopotentials and A. Darlington for fruitful discussions related to the lower-symmetry phases.

References

Akber-Knutson, S., Bukowinski, M. S. T. & Matas, J. (2002). *Geophys. Res. Lett.* **29**, 0.1029/2001GL013523.
Baroni, S., de Gironcoli, S., Dal Corso, A. & Gianozzi, P. (2001). *Rev. Mod. Phys.* **73**, 515–562.
Caracas, R., Wentzcovitch, R. M., Price, D. G. & Brodholt, J. (2005). *Geophys. Res. Lett.* **32**, 10.1029/2004GL022144.
Chizmeshya, A. V. G., Wolf, G. H. & McMillan, P. F. (1996). *Geophys. Res. Lett.* **23**, 2725–2728.
Darlington, C. N. W. (2002). *Acta Cryst.* A**58**, 66–71.
Froyen, S. (1992). *Phys. Rev. B*, **45**, 3796–3798.
Gasparik, T., Wolf, K. & Smith, C. M. (1994). *Am. Mineral.* **79**, 1219–1222.
Glazer, A. M. (1972). *Acta Cryst.* B**28**, 3384–3392.
Glazer, A. M. (1975). *Acta Cryst.* A**31**, 756–762.
Hohenberg, P. & Kohn, W. (1964). *Phys. Rev.* **136**, B864–B871.
Howard, C. J. & Stokes, H. T. (1998). *Acta Cryst.* B**54**, 782–789.
Ita, J. J. & Stixrude, L. (1992). *J. Geophys. Res.* **23**, 6849–6866.
Jung, D. Y. & Oganov, A. R. (2005). *Phys. Chem. Miner.* **32**, 146–153.
Karki, B. B. & Wentzcovitch, R. (2003). *Phys. Rev. B*, **68**, 224304–6.
Kohn, W. & Sham, L. J. (1965). *Phys. Rev. A*, **140**, 1133–1138.
Liu, L. & Ringwood, A. E. (1975). *Earth Planet. Sci. Lett.* **28**, 209–211.
Magyari-Köpe, B., Vitos, L., Grimvall, G., Johansson, B. & Kolåar, J. (2002). *Phys. Rev. B*, **65**, 193107.
Monkhorst, H. J. & Pack, J. D. (1976). *Phys. Rev. B*, **13**, 5188–5192.
O'Neill, B. & Jeanloz, R. (1990). *Geophys. Res. Lett.* **17**, 1477–1480.
Ringwood, A. E. (1975). *Composition and Petrology of the Earth's Mantle*, 618 pp. New York: McGraw-Hill.
Shim, S.-H., Duffy, T. S. & Shen, G. (2000). *J. Geophys. Res. B*, **105**, 25955–25968.
Shim, S.-H., Jeanloz, R. & Duffy, T. S. (2002). *Geophys. Res. Lett.* **29**, 2166–2169.
Stixrude, L., Cohen, R. E., Yu, R. & Krakauer, H. (1996). *Am. Mineral.* **81**, 1293–1296.
Swamy, V. & Dubrovinsky, L. S. (1997). *Geochim. Cosmochim. Acta*, **61**, 1181–1191.
Wang, Y. & Weidner, D. J. (1994). *Geophys. Res. Lett.*, **21**, 895–898.
Wentzcovitch, R. M. (1991). *Phys. Rev. B*, **44**, 23582361.